arXiv:1610.06277v1 [astro-ph.EP] 20 Oct 2016

The Near-Surface Methane Humidity on Titan

Accepted for publication in Icarus

Juan M. Lora[a], Máté Ádámkovics[b]

[a] *Department of Earth, Planetary and Space Sciences, University of California, Los Angeles, CA 90095, USA*
[b] *Astronomy Department, University of California, Berkeley, CA 94720, USA*

Abstract

We retrieve vertical and meridional variations of methane mole fraction in Titan's lower troposphere by re-analyzing near-infrared ground-based observations from 17 July 2014 UT (Ádámkovics et al., 2016). We generate synthetic spectra using atmospheric methane profiles that do not contain supersaturation or discontinuities to fit the observations, and thereby retrieve minimum saturation altitudes and corresponding specific humidities in the boundary layer. We relate these in turn to surface-level relative humidities using independent surface temperature measurements. We also compare our results with general circulation model simulations to interpret and constrain the relationship between humidities and surface liquids. The results show that Titan's lower troposphere is undersaturated at latitudes south of 60°N, consistent with a dry surface there, but increases in humidity toward the north pole indicate appreciable surface liquid coverage. While our observations are consistent with considerably more liquid methane existing at the north pole than is present in observed lakes, a degeneracy between low-level methane and haze leads to substantial uncertainty in determining the extent of the source region.

Keywords: Titan, atmosphere, Adaptive optics, Atmospheres, evolution, Atmospheres, structure

Email addresses: jlora@ucla.edu (Juan M. Lora), mate@berkeley.edu (Máté Ádámkovics)

1. Introduction

Like Earth, Titan experiences an active hydrologic cycle, which is responsible for the occurrence of tropospheric methane clouds (Brown et al., 2002; Griffith et al., 2005; Schaller et al., 2006, 2009), precipitation (Turtle et al., 2011), and resulting erosional surface features like channels and flood plains (Elachi et al., 2005; Tomasko et al., 2005; Lopes et al., 2010). Unlike on Earth, where the vast majority of water available to the climate system is in the ocean, Titan's observable methane is primarily in the atmosphere, which contains up to an order of magnitude more than the surface (Lorenz et al., 2008). Subsurface reservoirs are unknown, but since the atmospheric lifetime of methane is geologically short due to photolysis (Yung et al., 1984), we only have hypotheses (e.g., subsurface clathrates; Atreya et al., 2006) for the ultimate source of methane in the climate system. As a result, determination of the atmospheric methane content, particularly in the troposphere, is important and broadly interesting in the context of both the climate and atmospheric evolution.

Methane thermodynamics is an important component of the energy budget and circulation of Titan's atmosphere (Mitchell et al., 2006, 2009; Mitchell, 2012), and the methane humidity is a key factor in the development of convective cloud systems (Barth and Rafkin, 2007; Griffith et al., 2008). The distribution of methane in the atmosphere may be diagnostic of the methane at or near the surface (Mitchell, 2008; Lora et al., 2015): Because it is largely set by the availability of surface methane, the near-surface humidity is particularly important for determining the contemporary distribution of surface and subsurface methane, and its accessibility to the atmosphere. The *Huygens* Gas Chromatograph Mass Spectrometer (GCMS) measured a near-surface relative humidity of roughly 50% near the equator (Niemann et al., 2010), but the processes that set that value are as yet uncertain since the equatorial region is considered largely a desert (Griffith et al., 2014; Mitchell and Lora, 2016). Though it has been suggested that low-latitude fluvial erosional features could be relics of a rainier past (Griffith et al., 2008), potential paleolake basins at high latitudes (Hayes, 2016) and paleoclimate simulations (Lora et al., 2014) suggest that surface methane cycles between the poles on geologic timescales, rarely remaining at low latitudes. Yet there is evidence for present surface liquids at low latitudes (Griffith et al., 2012), so a fully consistent picture of Titan's hydrologic cycle remains elusive.

While the low latitudes are dry, Titan's poles support lakes of liquid hy-

drocarbons (Stofan et al., 2007; Hayes et al., 2008; Turtle et al., 2009), which may be connected hydraulically over regional scales by subsurface "alkanofers" (Hayes, 2016). These polar regions are also topographically depressed with respect to other latitudes, and relatively devoid of craters, which suggests the possibility of extensive high-latitude wetlands (Neish and Lorenz, 2014). Furthermore, surface temperature measurements from *Cassini* Composite Infrared Spectrometer (CIRS) suggest that, as springtime advances, the north pole has warmed more slowly than expected from a dry porous regolith (Jennings et al., 2016). And despite the northern lakes occupying only about 10% of the polar surface (Hayes et al., 2011), no zonal temperature contrasts have been detected, which is interpreted as further indication of moist ground (Jennings et al., 2016). Such circumstantial evidence raises the question: Do the lakes represent the entire source region of methane that enters the atmosphere, or is there a larger geographical region with moisture seeping out of the regolith?

Initial studies of the methane cycle in general circulation models of Titan's atmosphere assumed an infinite supply of surface methane globally available to the atmosphere (Rannou et al., 2006; Mitchell et al., 2006), but more recent work has shown that the atmospheric circulation transports methane to the poles, where it is cold-trapped (Mitchell, 2008; Schneider et al., 2012; Lora et al., 2015; Lora and Mitchell, 2015), and the simulations that are most consistent with various observations are those where the rest of the surface is largely dry (Lora et al., 2015). In short, the interactions of surface liquids with the atmosphere, and subsurface processes affecting these liquids, are only roughly parameterized in models, and very few observations are available as benchmarks. An understanding of the distribution of low-level humidity on Titan would shed some light on these issues, but measurements of the variation of humidity with latitude have been limited and considerably hindered by Titan's opaque and nearly-saturated atmosphere (Anderson et al., 2008; Penteado et al., 2010).

Recently, Ádámkovics et al. (2016) used high spectral resolution observations in the near-IR—with complementary lower-resolution and wider bandpass measurements to constrain spatial variations in haze opacity—to measure the meridional variation of tropospheric methane. Their simultaneous ground-based observations from two facilities were unable to break a degeneracy between the roughly anti-correlated methane (absorption) and haze (scattering) opacities near the surface, leading to ambiguity in determining whether the methane or haze near the surface was variable. Simulated

images of *Cassini* VIMS observations of both northern and southern hemispheres suggest that a spatially uniform near-surface haze is more likely, and circulation models with haze microphysics support this interpretation, since they predict that haze near the surface should not have strong spatial variations (Larson et al., 2014). A uniform surface haze means that the observed opacity variations near the surface are indeed due to changes in the methane content.

Our motivation here is to measure and interpret the distribution of near-surface methane in Titan's atmosphere, specifically by considering both the vertical and meridional variation in atmospheric methane. Ádámkovics et al. (2016) implemented an ad hoc scale factor for the methane profile in the troposphere, which lead to supersaturated conditions in retrieved profiles with relatively high column methane content. Here we invoke a realistic variation in the vertical mole fraction of methane, which does not allow supersaturation, in order to interpret high-resolution near-IR spectra. We describe our observational and radiative methods in Section 2.1, and the models used for interpreting these data in Section 2.2. Results are presented in Section 3, and we discuss how our methods leverage the increased sensitivity to opacity variations at higher altitudes and connect them in a physical way to near-surface humidities, as well as how assumptions about the surface temperature are important for retrieving relative humidities. We describe how well our observations constrain the distribution of methane on the surface in Section 4.

2. Methods

2.1. Observations and Simulated Spectra

The Near-InfraRed SPectrometer (McLean et al., 1998) with Adaptive Optics (NIRSPAO) was used at W. M. Keck Observatory on 17 July 2014 UT to observe Titan with a spectral resolving power of $R \approx 25,000$ and a spatial sampling of 0.018"/pixel along the slit. A single north-to-south position along the central meridian was integrated for 45 min. We analyze spectra from one echelle order centered near 1.55 μm. Additional details of these observations, including the data reduction and calibration with supporting datasets, are described in Ádámkovics et al. (2016).

Synthetic spectra are generated by defining 20 atmospheric layers, with properties that are determined primarily by measurements made with instruments on the *Huygens* probe (HASI and GCMS instruments; see be-

low), including the temperature, pressure, methane mole fraction, and haze structure. These *in situ* measurements are used to determine the gas and scattering opacity in each layer of the model. The discrete ordinate method radiative transfer (DISORT; Stamnes et al., 1988) is implemented in Python (PyDISORT) and used to solve the radiative transfer through the model atmosphere and simulate the observed flux. The methane in the lower atmosphere and haze in the upper atmosphere are assumed to vary with latitude (Ádámkovics et al., 2016); however, here we consider a more physically realistic vertical (altitude) structure for the methane gas, which is used to determine the methane relative humidity, RH, at the surface.

The vertical profile of methane measured by the GCMS experiment on the *Huygens* probe follows the saturation curve from roughly 40 km down to 6 km altitude, below which the methane mole fraction is constant at 0.057 (Niemann et al., 2010). In order to explain its meridional variation, Ádámkovics et al. (2016) consider a methane profile that scales the tropospheric methane mole fraction below 35 km altitude. While straightforward, making such an assumption has limitations. For example, in order to accommodate an increase in methane opacity, this assumption leads to supersaturation at altitudes above 6 km. It is also unclear if the changes in the synthetic spectra from such a variation are most sensitive to higher or lower altitude methane mole fraction changes. While the number density of methane is largest near the surface, and therefore should contribute the greatest amount to the total column, there are wavelength windows that are insensitive to the surface. These windows become wider in wavelength near the limb, where the slant paths through the atmosphere and therefore the total opacity are larger. Lastly, scaling the methane mole fraction leads to a discontinuity at 35 km altitude, the level used to identify the top of the troposphere.

Here we avoid the supersaturation of methane and discontinuities in the retrieved methane mole fraction by considering profiles that have a characteristic minimum altitude of saturation, z_s. We consider z_s a free parameter for fitting synthetic spectra to the observations. If a greater methane opacity is required to fit the observations, we increase the column of methane by decreasing the saturation altitude, rather than scaling the methane mole fraction at all altitudes. Conversely, in order to decrease the column of methane, we increase z_s. The methane saturation vapor pressure at temperature T is given by the Clausius-Clapeyron relation over a binary mixture with saturation vapor pressure 106 mbar at 90.7 K (Thompson et al., 1992; Lora et al.,

2015):

$$p_s(T) = X_{\mathrm{CH4}} * 106. * \exp(L_v/R_d * ((1.0/90.7) - (1.0/T))), \quad (1)$$

where L_v and R_d are the latent heat of evaporation (assumed constant) and gas constant for methane, respectively. $X_{\mathrm{CH4}} = 0.9$ is the fraction of methane in a methane-nitrogen mixture that best fits the GCMS data. We use the temperature profile measured by HASI on the *Huygens* probe to identify the temperature at a given altitude, $T(z)$ (Fulchignoni et al., 2005). Variations in the vertical profiles of methane are illustrated in Fig. 1. These profiles provide a more physically plausible variation in the total methane column than those used by Ádámkovics et al. (2016).

An example of a spectrum from a single pixel along the spectrometer slit is shown together with a best fit synthetic spectrum in Fig. 2. In this case, increasing or decreasing z_s leads to residuals that are in excess of estimates of the observational uncertainty. We determine the best value of z_s for each latitude (i.e., spatial pixel along the slit) by using a brute-force approach where we set z_s to the center of each layer of the model between 0 and 20 km altitude, generate synthetic spectra for each case, and calculate the mean squared residual, $\widehat{\chi^2}(z_s)$, between each synthetic spectrum and the observation. This process is repeated for spectra from each pixel along the slit.

2.2. Titan Atmospheric Model

We interpret the retrieved profiles in the context of Titan's climate and general circulation by comparison to simulations with the Titan Atmospheric Model (TAM), a three-dimensional general circulation model (GCM) that includes parameterizations for nongray radiative transfer, Titan's hydrologic cycle, surface, and boundary layer (Lora et al., 2015). A simple "bucket" model, wherein surface methane at each gridbox is replenished by precipitation and is available to evaporate into the atmosphere as long as it is above a minimum value, is used to represent surface/subsurface hydrology; no horizontal surface/subsurface transport occurs. The simulations here use a 32-layer (L32) atmosphere (Lora et al., 2015) at T42 resolution (approximately 2.8° resolution).

As a baseline and for comparison of our results to previous GCM simulations that either prescribed the surface humidity or assumed an infinite surface methane reservoir (Mitchell et al., 2006; Rannou et al., 2006;

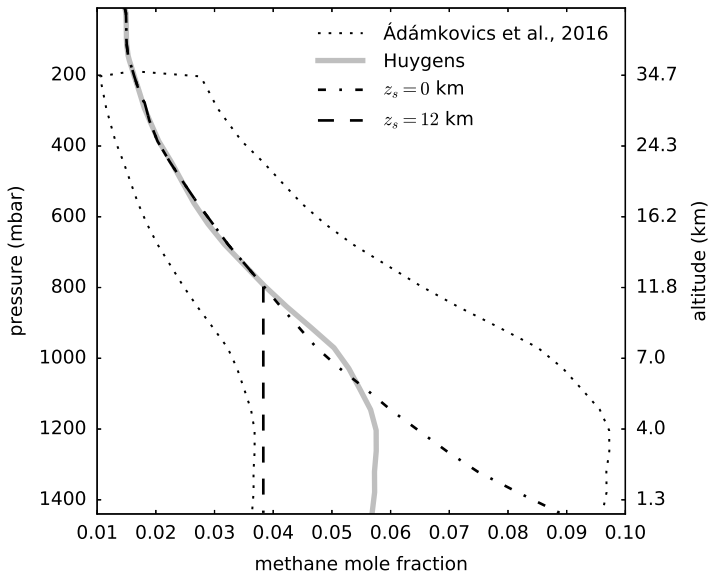

Figure 1: The methane mole fraction vertical profiles used in Ádámkovics et al. (2016) for changes to the total methane humidity (dotted) scale the *Huygens* profile (gray) below ∼200 mbar. This scaling causes supersaturation and an unphysical discontinuity. These profiles are compared with profiles that are defined by a characteristic minimum saturation altitude, z_s. Two examples are illustrated: saturation to the surface, z_s=0 (dash-dot), and a minimum saturation altitude of z_s=11 km altitude (dashed). The methane mole fraction is assumed to be constant below z_s, similar to the *Huygens* profile near the surface.

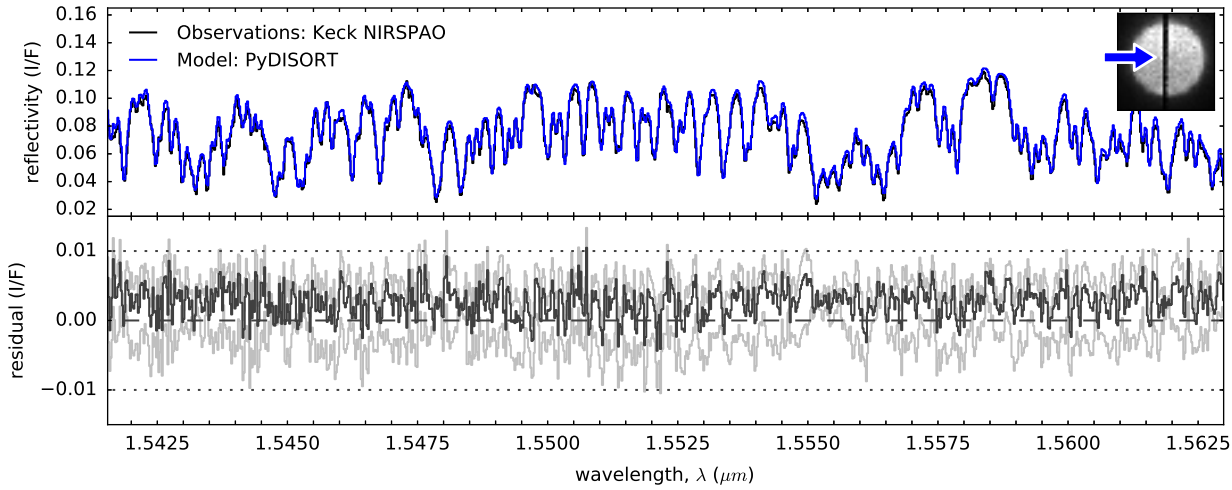

Figure 2: The spectrum from one NIRSPAO pixel (top panel; black), at the location specified by the blue arrow in the slit-viewing camera image (inset), is compared with the radiative transfer model spectrum (blue). The residuals are plotted in the bottom panel, with the ordinate scale magnified relative to the top panel. Residuals from radiative transfer models with minimum saturation altitudes that are either higher or lower in the atmosphere (gray) illustrate the spectral sensitivity to this parameter.

Tokano, 2009), we consider an "aquaplanet" scenario in which practically inexhaustible surface methane liquid is available globally. We also use results from previous (T21) simulations (Lora et al., 2015) in which only the locations of the largest observed lakes contain large amounts of surface methane, but other regions are allowed to moisten and dry self-consistently. Finally, we employ simulations following the "wetlands" scenario used in Lora and Mitchell (2015) and motivated by Neish and Lorenz (2014), where ample surface liquid is initialized poleward of 60° in both hemispheres. Under this configuration, we use a range of simulations varying the calculation of methane saturation vapor pressure to facilitate a more exhaustive comparison between simulation results and the observation analysis outlined above. These include parameterizations that include both liquid-vapor and ice-vapor phase transitions (i.e., simulations in Lora and Mitchell, 2015), or that assume only the liquid-vapor phase transition over liquid (Eq. 1) with a range of 80%–100% methane content ($X_{\mathrm{CH4}} = 0.8$–1.0).

Fig. 3 shows the zonal-mean surface-level specific humidities from the various TAM simulations during late northern spring, corresponding to the time of the observations. At low latitudes, the "wetlands" and "observed lakes" cases coincide in simulating lower specific humidities than at high latitudes, though in the latter case the contrast is considerably smaller as a result of the sparse coverage of polar liquids. In contrast, the "aquaplanet" case predicts the highest specific humidities near the equator, reflecting the global liquid coverage and peak annual-mean evaporation (responding to insolation) occurring at low latitudes. For comparison, the GCMS measurement (Fig. 1) corresponds to a surface value of specific humidity of roughly 0.032 kg kg^{-1} at 10°S, though at a different season from our observations.

The corresponding surface-level relative humidities from the simulations (right panel of Fig. 3) further accentuate the differences between the various simulated cases. The range of "wetland" cases bridges the high- and low-latitude predictions from the "aquaplanet" and "observed lakes" configurations with saturated conditions near the poles and much lower humidities at low latitudes, while the latter simulations predict consistently saturated ($RH \approx 100\%$) or undersaturated ($RH < 75\%$) conditions, respectively. The qualitatively different curves in Fig. 3 illustrate the ability of near-surface humidity measurements to distinguish between possible scenarios of the surface methane distribution on Titan.

Relative humidity depends strongly on temperature as well as specific humidity. The surface-level temperatures from the simulations at the season of

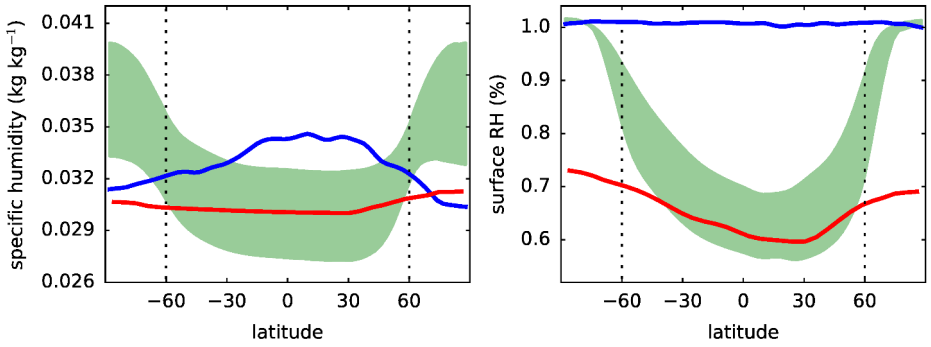

Figure 3: The simulated surface specific humidities at the season of the observations (left). The green area shows the range of results for "wetlands" simulations with various saturation parameterizations, including those from Lora and Mitchell (2015). Blue and red curves show simulations under "aquaplanet" and "observed" lake configurations (Lora et al., 2015), respectively. The corresponding surface-level relative humidities from the various TAM simulations (right) for the season of the observations. Colors are the same as in the left panel. Dotted vertical lines mark the edges of "wetlands."

observations are shown in Fig. 4, along with minimum surface temperatures derived from *Cassini* CIRS observations between 2013 and 2014 (Jennings et al., 2016). As discussed in Lora et al. (2015), the considerably smaller equator-to-pole contrast in the "aquaplanet" case compared to the observed temperatures refutes the possibility of global surface liquid existing on Titan. On the other hand, the rest of the simulations largely succeed in reproducing the temperature observations barring relatively minor discrepancies, lending confidence to the usefulness of comparison between retrieved and simulated relative humidities in these cases.

3. Results

Retrievals of the minimum saturation altitude z_s for all latitudes observed along the slit recover the meridional variation in methane mole fraction reported by Ádámkovics et al. (2016). Fig. 5 illustrates that the trend of increasing methane toward the southern latitudes and north pole corresponds to a decreasing minimum saturation altitude in these regions. Retrievals from the few pixels closest to the poles are consistent with saturated profiles down

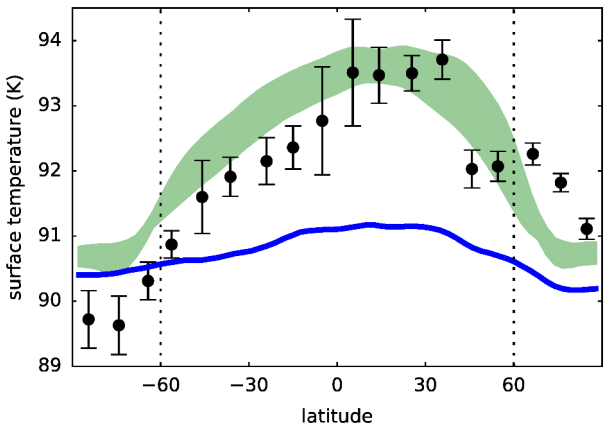

Figure 4: The zonal-mean surface temperatures corresponding to the time of the observations. Green area shows the range of results for both "wetlands" and "observed lakes" simulations; blue curve shows the "aquaplanet" simulation. Dotted vertical lines mark the edges of "wetlands." Black points with error bars show surface brightness temperatures measured between April 2013 and September 2014 by *Cassini* CIRS (Jennings et al., 2016).

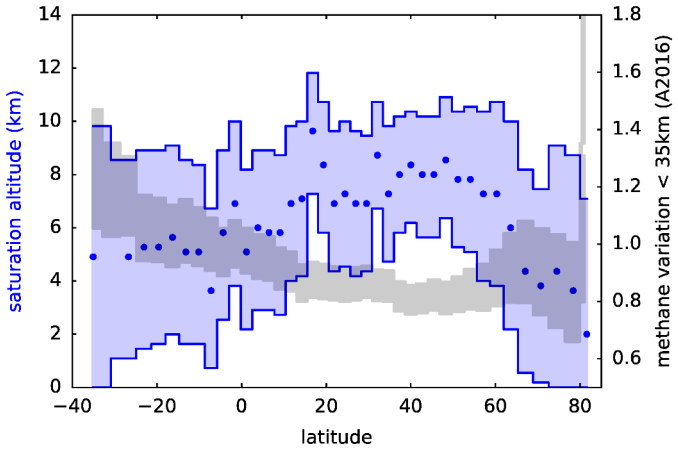

Figure 5: The minimum saturation altitude z_s determined by fitting spectra observed on 17 July 2014 UT at each location along the slit (blue) compared to the methane variation presented in Ádámkovics et al. (2016) (gray). Regions that were reported to have increased (decreased) tropospheric methane correspond to lower (higher) saturation altitudes. The sub-observer longitude is 291°W.

to the surface; however, the large slant path through the atmosphere near the observed limb of Titan means that the sensitivity to the near-surface is reduced as the total opacity from both scattering and gas absorption increase.

As described in Ádámkovics et al. (2016) and discussed in the following section, there is a degeneracy between the opacity due to methane and haze near the surface. We consider several scenarios for the retrievals, which are outlined in the Appendix. We find that in the cases where the low-altitude haze opacity is allowed to vary, the degeneracy in the opacities removes meridional variations in the retrieved saturation altitudes. However, simulated images of *Cassini* VIMS observations in both northern and southern hemispheres suggest that a uniform near-surface haze is more likely (Ádámkovics et al., 2016). Moreover, predictions from circulation models that include haze microphysics (Rannou et al., 2004; Larson et al., 2014) indicate little meridional variability in the haze in the lower troposphere. Nevertheless, in the following we also consider the retrievals with variable low-level haze.

Assuming a constant tropospheric haze opacity, the retrieved saturation

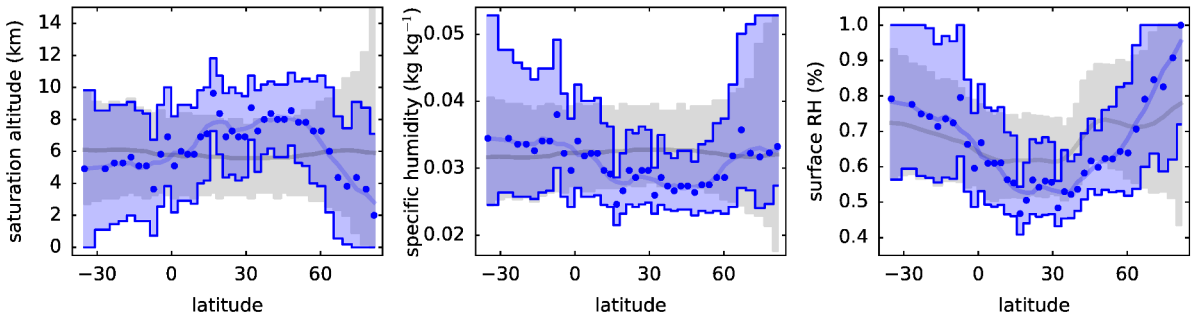

Figure 6: The meridional variation of minimum saturation altitudes (left), corresponding specific humidities (middle), and associated surface-level relative humidities (right) retrieved from the observations. Retrievals assuming a constant haze opacity (see text) are shown in blue, while retrievals assuming a variable haze opacity are shown in gray. Curves of the running mean of the retrieved values are shown for ease of comparison.

altitudes in the southern hemisphere are roughly constant, with the minimum $\widehat{\chi}^2(z_s)$ suggesting values of between 5 and 6 km, in agreement with the value inferred from *in situ* observations (Niemann et al., 2010). These increase to about 8 km in the low latitude northern hemisphere, where they are also roughly constant between 15° and 50°N. Poleward of this, there is a pronounced turnover in the retrievals as the saturation altitudes drop from ∼7 to ∼4 km around 60°N, and the lowest values occur nearest the north pole. In the cases where the tropospheric haze opacity is assumed to be variable (Fig. 6), the preferred saturation altitudes are essentially constant at 6 km at all latitudes, but with increasing uncertainties toward the north that are consistent with both increasing and decreasing values, including saturation at the surface near the north pole. Similar uncertainties are not present toward the southern hemisphere, and in this case the values are constrained to within the same range as in the low latitude northern hemisphere.

The variation with latitude of the specific humidity associated with the retrieved minimum saturation altitudes is consistent with higher low-level moisture content in the southern hemisphere as well as the north polar region, with a minimum at the low- to mid-latitudes of the northern hemisphere in the case of constant haze opacity (Fig. 6, center panel). With the possible exception of a few locations, we retrieve values for the surface specific

humidity in these regions that are the same (within error) to that measured by the GCMS on *Huygens* at 10°S. The same is true of specific humidities retrieved assuming a variable haze, in which case the values are more constant with latitude but again are consistent with considerable variations at high northern latitudes, up to a ∼60% enhancement near the pole.

Taking the specific humidity to be nearly constant in the sub-saturated layer below the altitude of saturation (see Fig. 1), the above retrievals can be combined with independent observational estimates of the surface temperatures (Fig. 4) to yield the surface-level relative humidities. In both haze opacity cases, the resulting relative humidity variations with latitude occur in a wide "U" shape that mostly results from the variation of surface temperatures. Nevertheless, the values from northern mid-latitudes to the south are mostly consistent with a sub-saturated lower troposphere, with the lowest relative humidities at the latitudes of peak temperatures (in agreement with the simulations, Fig. 3). In the southern hemisphere, the two retrievals are consistent with each other, but the lowest relative humidities are roughly 10% lower in the case of constant haze opacity in the region of highest temperatures, roughly 15°–45°N. This case also exhibits a considerable variation toward the north pole, with preferred values surpassing 80% relative humidity at latitudes north of 60°N. In both cases, the profiles are consistent with low-level saturation in the northern polar regions.

Fig. 7 compares the retrieved surface-level specific and relative humidities to those simulated by TAM. Despite the considerable uncertainties, the meridional variations of the specific humidity from the observations are compatible with the "wetlands" simulations, with the lowest values occurring at northern mid-latitudes (during the northern spring season), and increasing humidities toward the north pole. The associated relative humidities display similar—though more pronounced—meridional trends, with considerable low-level sub-saturation at low- and mid-latitudes, and increasing saturation toward the north pole.

4. Discussion

Comparison of the retrieved to simulated near-surface methane humidities (cf. Figs. 3 and 6) convincingly eliminates the "aquaplanet" scenario as a plausible configuration for Titan's surface liquids, which calls into question the details of hydrologic cycles simulated by models that prescribe excessive surface methane at low latitudes. However, while the high-latitude "wet-

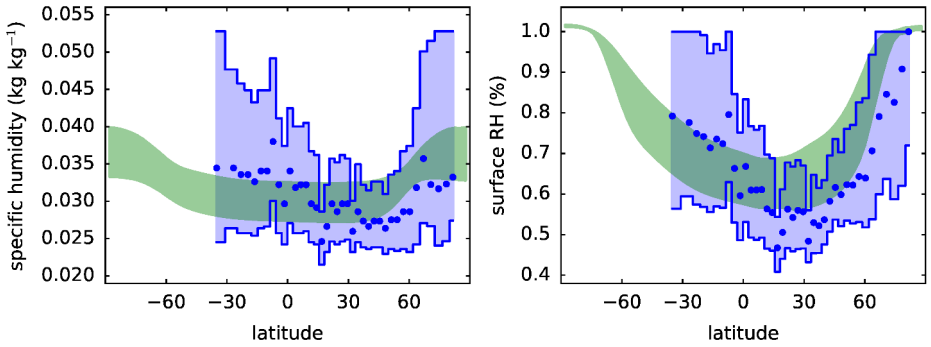

Figure 7: Comparison of the retrieved and simulated specific (left) and relative (right) humidities near the surface. Blue points with uncertainty envelopes are the same as in Fig. 6, while the green areas are the simulation results as in Fig. 3.

lands" distribution is compatible with the retrievals (Fig. 7), we cannot conclusively rule out the possibility that Titan's surface methane available to the atmosphere exists exclusively in the observed northern lakes; the "observed lakes" simulation falls in the lower values of humidity within the retrievals' uncertainties.

With the constraints provided by our observations and simulations, it is straightforward to interpret the increase in the near-surface humidity at the north pole as a consequence of the existence of surface liquids there, whether or not they are more extensive than the observed lakes. This implies that such surface methane humidifies the regional boundary layer, which in turn transports its moisture to lower latitudes as a result of atmospheric dynamics (Lora and Mitchell, 2015; Mitchell and Lora, 2016). As a corollary, the northern polar near surface should increase its methane humidity as the seasons progress toward summer solstice and evaporation from the lake surfaces intensifies, likely triggering convective cloud activity if the overlying troposphere is sufficiently unstable.

Conversely, it is difficult to reconcile the apparent retrieved increase in near-surface humidity toward the southern hemisphere (in the constant haze opacity case) with any of the simulations. Ádámkovics et al. (2016) interpret the increase in column methane toward the south pole, approaching winter at the time of the observations, as possibly arising from evaporation from

moist ground, as Ontario Lacus is a vastly insufficient source of methane and such an increase implies distinct source regions of methane vapor in the two hemispheres. But even the TAM "wetlands" simulation, with surface methane covering the entire south pole, is only marginally consistent with the retrieved specific humidities toward the south (Fig. 7). Two possibilities emerge as solutions to this conundrum: Either much more of the southern hemisphere is covered in liquid (possibly down to the low latitudes), or the assumption of constant low-level haze opacity begins to fail in the southern hemisphere. An inherent problem with the former option is that such a liquid distribution would push the system closer to the "aquaplanet" configuration, which is incompatible with observations of Titan's surface (Stofan et al., 2007; Lorenz et al., 2006; Mitchell and Lora, 2016), so we are left to conclude that the observational uncertainties toward the south preclude a determination of the meridional variation of low-level atmospheric methane there.

As a result, a conservative interpretation is that Titan's near-surface meridional humidity variations roughly fall in the areas of overlap of the uncertainty envelopes of our two end-member retrievals. As such, low-latitude variations are difficult to make out, but the increase in humidity toward the north pole is a more robust feature (though with still substantial uncertainties). The same general trend is true of the "wetlands" simulations, where subtle low-latitude variations of humidity give way to large increases toward the polar regions.

From late 2006 through early 2007, Brown et al. (2009) measured low-altitude fog near the south pole, indicating a saturated atmosphere above the surface. There did not seem to be a correlation with the location of Ontario Lacus, and the meteorological conditions giving rise to the observed phenomenon remain unknown. If we speculate that the existence and location of fog, like higher-altitude clouds, are seasonally variable, and further assume that the meteorology of the north and south poles are similar, then saturated conditions near the surface at the north pole may be consistent with the formation of fog there. Predictions from circulation models suggest that analogs of the large clouds seen during southern summer should already be occuring near the north pole; it is unclear if the current absence of prominent convective clouds near the north pole is related to the possibility of saturated conditions and the stability of the troposphere.

Future near-IR observations used to measure the methane content near the surface will continue to face the challenge of differentiating between the opacity due to methane absorption and that due to haze scattering. This de-

generacy exists even though the methane spectrum in the near-IR is highly variable with wavelength, while the haze opacity is not. The difficulty arises from the fact that in the spectral regions where methane opacity is low (and the reflectivity is high)—wavelengths that are sensitive to atmospheric opacity down to the surface—an increase (decrease) in the methane mole fraction leads to changes in the reflectivity spectrum that are similar to a decrease (increase) in the haze opacity. The many weak, densely-spaced, and pressure-broadened methane line wings contribute to a pseudo-continuum in the methane line opacity.

While very high S/N observations may be able to resolve the differences in line wing shapes due to methane variation from those due to haze variation, it is unclear whether systematic instrumental uncertainties will limit the S/N that can be achieved. Spectra at longer wavelengths, approaching the mid-IR, have less densely spaced methane lines, which suggests that there may be a better chance of resolving line profiles that are sensitive to the methane content near the surface. However, telluric thermal emission makes ground-based observation of Titan at these wavelengths prohibitively difficult. Combining simultaneous observations in the visible, near- and mid-IR, at both low and high scattering phase angles could probe both the methane and haze opacity in a way that might break the degeneracy for methane retrievals.

Acknowledgements

The authors thank D. Jennings for providing surface temperature measurements, and J. Mitchell for important discussions. M.Á. was supported by NASA grant NNX14AG82G.

References

References

Ádámkovics, M., Barnes, J. W., Hartung, M., de Pater, I., Aug. 2010. Observations of a stationary mid-latitude cloud system on Titan. Icarus 208, 868–877.

Ádámkovics, M., Mitchell, J. L., Sep. 2016. Search for methane isotope fractionation due to Rayleigh distillation on Titan. Icarus 275, 232–238.

Ádámkovics, M., Mitchell, J. L., Hayes, A. G., Rojo, P. M., Corlies, P., Barnes, J. W., Ivanov, V. D., Brown, R. H., Baines, K. H., Buratti, B. J., Clark, R. N., Nicholson, P. D., Sotin, C., May 2016. Meridional variation in tropospheric methane on Titan observed with AO spectroscopy at Keck and VLT. Icarus 270, 376–388.

Anderson, C. M., Young, E. F., Chanover, N. J., McKay, C. P., Apr. 2008. HST spectral imaging of Titan's haze and methane profile between 0.6 and 1 μm during the 2000 opposition. Icarus 194, 721–745.

Atreya, S. K., Adams, E. Y., Niemann, H. B., Demick-Montelara, J. E., Owen, T. C., Fulchignoni, M., Ferri, F., Wilson, E. H., Oct. 2006. Titan's methane cycle. Planet. Space Sci. 54, 1177–1187.

Barth, E. L., Rafkin, S. C. R., Feb. 2007. TRAMS: A new dynamic cloud model for Titan's methane clouds. Geophys. Res. Lett. 34 (3), L03203.

Brown, M. E., Bouchez, A. H., Griffith, C. A., Dec. 2002. Direct detection of variable tropospheric clouds near Titan's south pole. Nature 420, 795–797.

Brown, M. E., Smith, A. L., Chen, C., Ádámkovics, M., Nov. 2009. Discovery of Fog at the South Pole of Titan. ApJ 706 (1), L110–L113.

Elachi, C., Wall, S., Allison, M., Anderson, Y., Boehmer, R., Callahan, P., Encrenaz, P., Flamini, E., Franceschetti, G., Gim, Y., Hamilton, G., Hensley, S., Janssen, M., Johnson, W., Kelleher, K., Kirk, R., Lopes, R., Lorenz, R., Lunine, J., Muhleman, D., Ostro, S., Paganelli, F., Picardi, G., Posa, F., Roth, L., Seu, R., Shaffer, S., Soderblom, L., Stiles, B., Stofan, E., Vetrella, S., West, R., Wood, C., Wye, L., Zebker, H., May 2005. Cassini Radar Views the Surface of Titan. Science 308, 970–974.

Fulchignoni, M., Ferri, F., Angrilli, F., Ball, A. J., Bar-Nun, A., Barucci, M. A., Bettanini, C., Bianchini, G., Borucki, W., Colombatti, G., Coradini, M., Coustenis, A., Debei, S., Falkner, P., Fanti, G., Flamini, E., Gaborit, V., Grard, R., Hamelin, M., Harri, A. M., Hathi, B., Jernej, I., Leese, M. R., Lehto, A., Lion Stoppato, P. F., López-Moreno, J. J., Mäkinen, T., McDonnell, J. A. M., McKay, C. P., Molina-Cuberos, G., Neubauer, F. M., Pirronello, V., Rodrigo, R., Saggin, B., Schwingenschuh, K., Seiff, A., Simões, F., Svedhem, H., Tokano, T., Towner, M. C., Trautner, R., Withers, P., Zarnecki, J. C., Dec. 2005. In situ measurements of the physical characteristics of Titan's environment. Nature 438, 785–791.

Griffith, C. A., Lora, J. M., Turner, J., Penteado, P. F., Brown, R. H., Tomasko, M. G., Doose, L., See, C., Jun. 2012. Possible tropical lakes on Titan from observations of dark terrain. Nature 486, 237–239.

Griffith, C. A., McKay, C. P., Ferri, F., Nov. 2008. Titan's Tropical Storms in an Evolving Atmosphere. ApJ 687, L41–L44.

Griffith, C. A., Penteado, P., Baines, K., Drossart, P., Barnes, J., Bellucci, G., Bibring, J., Brown, R., Buratti, B., Capaccioni, F., Cerroni, P., Clark, R., Combes, M., Coradini, A., Cruikshank, D., Formisano, V., Jaumann, R., Langevin, Y., Matson, D., McCord, T., Mennella, V., Nelson, R., Nicholson, P., Sicardy, B., Sotin, C., Soderblom, L. A., Kursinski, R., Oct. 2005. The Evolution of Titan's Mid-Latitude Clouds. Science 310, 474–477.

Griffith, C. A., Rafkin, S., Rannou, P., McKay, C. P., 2014. Storms, clouds, and weather. In: Müller-Wodarg, I., Griffith, C. A., Lellouch, E., Cravens, T. E. (Eds.), Titan: Interior, surface, atmosphere, and space environment. Cambridge University Press, Cambridge.

Hayes, A., Aharonson, O., Callahan, P., Elachi, C., Gim, Y., Kirk, R., Lewis, K., Lopes, R., Lorenz, R., Lunine, J., Mitchell, K., Mitri, G., Stofan,

E., Wall, S., May 2008. Hydrocarbon lakes on Titan: Distribution and interaction with a porous regolith. Geophys. Res. Lett. 35, L9204.

Hayes, A. G., 2016. The lakes and seas of Titan. Ann. Rev. Earth Planet. Sci. 44 (1), in press.

Hayes, A. G., Aharonson, O., Lunine, J. I., Kirk, R. L., Zebker, H. A., Wye, L. C., Lorenz, R. D., Turtle, E. P., Paillou, P., Mitri, G., Wall, S. D., Stofan, E. R., Mitchell, K. L., Elachi, C., Cassini Radar Team, Jan. 2011. Transient surface liquid in Titan's polar regions from Cassini. Icarus 211, 655–671.

Jennings, D. E., Cottini, V., Nixon, C. A., Achterberg, R. K., Flasar, F. M., Kunde, V. G., Romani, P. N., Samuelson, R. E., Mamoutkine, A., Gorius, N. J. P., Coustenis, A., Tokano, T., Jan. 2016. Surface Temperatures on Titan during Northern Winter and Spring. ApJ 816, L17.

Larson, E. J. L., Toon, O. B., Friedson, A. J., 2014. Simulating Titan's aerosols in a three dimensional general circulation model. Icarus 243, 400–419.

Lopes, R. M. C., Stofan, E. R., Peckyno, R., Radebaugh, J., Mitchell, K. L., Mitri, G., Wood, C. A., Kirk, R. L., Wall, S. D., Lunine, J. I., Hayes, A., Lorenz, R., Farr, T., Wye, L., Craig, J., Ollerenshaw, R. J., Janssen, M., Legall, A., Paganelli, F., West, R., Stiles, B., Callahan, P., Anderson, Y., Valora, P., Soderblom, L., The Cassini Radar Team, Feb. 2010. Distribution and interplay of geologic processes on Titan from Cassini radar data. Icarus 205, 540–558.

Lora, J. M., Lunine, J. I., Russell, J. L., Apr. 2015. GCM simulations of Titan's middle and lower atmosphere and comparison to observations. Icarus 250, 516–528.

Lora, J. M., Lunine, J. I., Russell, J. L., Hayes, A. G., Nov. 2014. Simulations of Titan's paleoclimate. Icarus 243, 264–273.

Lora, J. M., Mitchell, J. L., Aug. 2015. Titan's asymmetric lake distribution mediated by methane transport due to atmospheric eddies. Geophys. Res. Lett. 42, 6213–6220.

Lorenz, R. D., Mitchell, K. L., Kirk, R. L., Hayes, A. G., Aharonson, O., Zebker, H. A., Paillou, P., Radebaugh, J., Lunine, J. I., Janssen, M. A., Wall, S. D., Lopes, R. M., Stiles, B., Ostro, S., Mitri, G., Stofan, E. R., Jan. 2008. Titan's inventory of organic surface materials. Geophys. Res. Lett. 35, 2206.

Lorenz, R. D., Wall, S., Radebaugh, J., Boubin, G., Reffet, E., Janssen, M., Stofan, E., Lopes, R., Kirk, R., Elachi, C., Lunine, J., Mitchell, K., Paganelli, F., Soderblom, L., Wood, C., Wye, L., Zebker, H., Anderson, Y., Ostro, S., Allison, M., Boehmer, R., Callahan, P., Encrenaz, P., Ori, G. G., Francescetti, G., Gim, Y., Hamilton, G., Hensley, S., Johnson, W., Kelleher, K., Muhleman, D., Picardi, G., Posa, F., Roth, L., Seu, R., Shaffer, S., Stiles, B., Vetrella, S., Flamini, E., West, R., May 2006. The Sand Seas of Titan: Cassini RADAR Observations of Longitudinal Dunes. Science 312, 724–727.

McLean, I. S., Becklin, E. E., Bendiksen, O., Brims, G., Canfield, J., Figer, D. F., Graham, J. R., Hare, J., Lacayanga, F., Larkin, J. E., Larson, S. B., Levenson, N., Magnone, N., Teplitz, H., Wong, W., Aug. 1998. Design and development of NIRSPEC: a near-infrared echelle spectrograph for the Keck II telescope. In: Fowler, A. M. (Ed.), Infrared Astronomical Instrumentation. Vol. 3354 of Society of Photo-Optical Instrumentation Engineers (SPIE) Conference Series. pp. 566–578.

Mitchell, J. L., Aug. 2008. The drying of Titan's dunes: Titan's methane hydrology and its impact on atmospheric circulation. J. Geophys. Res. Planets 113 (E12), E08015.

Mitchell, J. L., Sep. 2012. Titan's Transport-driven Methane Cycle. ApJ 756, L26.

Mitchell, J. L., Lora, J. M., 2016. The climate of Titan. Ann. Rev. Earth Planet. Sci. 44 (1), in press.

Mitchell, J. L., Pierrehumbert, R. T., Frierson, D. M. W., Caballero, R., December 2006. The dynamics behind titan's methane clouds. PNAS 103 (49), 18421–18426.

Mitchell, J. L., Pierrehumbert, R. T., Frierson, D. M. W., Caballero, R., Sep. 2009. The impact of methane thermodynamics on seasonal convection and circulation in a model Titan atmosphere. Icarus 203, 250–264.

Neish, C. D., Lorenz, R. D., Jan. 2014. Elevation distribution of Titan's craters suggests extensive wetlands. Icarus 228, 27–34.

Niemann, H. B., Atreya, S. K., Demick, J. E., Gautier, D., Haberman, J. A., Harpold, D. N., Kasprzak, W. T., Lunine, J. I., Owen, T. C., Raulin, F., Dec. 2010. Composition of Titan's lower atmosphere and simple surface volatiles as measured by the Cassini-Huygens probe gas chromatograph mass spectrometer experiment. J. Geophys. Res. Planets 115 (E14), 12006.

Penteado, P. F., Griffith, C. A., Tomasko, M. G., Engel, S., See, C., Doose, L., Baines, K. H., Brown, R. H., Buratti, B. J., Clark, R., Nicholson, P., Sotin, C., Mar. 2010. Latitudinal variations in Titan's methane and haze from Cassini VIMS observations. Icarus 206, 352–365.

Rannou, P., Hourdin, F., McKay, C. P., Luz, D., Aug. 2004. A coupled dynamics-microphysics model of Titan's atmosphere. Icarus 170, 443–462.

Rannou, P., Montmessin, F., Hourdin, F., Lebonnois, S., Jan. 2006. The Latitudinal Distribution of Clouds on Titan. Science 311, 201–205.

Schaller, E. L., Brown, M. E., Roe, H. G., Bouchez, A. H., May 2006. A large cloud outburst at Titan's south pole. Icarus 182, 224–229.

Schaller, E. L., Roe, H. G., Schneider, T., Brown, M. E., Aug. 2009. Storms in the tropics of Titan. Nature 460, 873–875.

Schinder, P. J., Flasar, F. M., Marouf, E. A., French, R. G., McGhee, C. A., Kliore, A. J., Rappaport, N. J., Barbinis, E., Fleischman, D., Anabtawi, A., Nov. 2012. The structure of Titan's atmosphere from Cassini radio occultations: Occultations from the Prime and Equinox missions. Icarus 221, 1020–1031.

Schneider, T., Graves, S. D. B., Schaller, E. L., Brown, M. E., Jan. 2012. Polar methane accumulation and rainstorms on Titan from simulations of the methane cycle. Nature 481, 58–61.

Stamnes, K., Tsay, S.-C., Jayaweera, K., Wiscombe, W., 1988. Numerically stable algorithm for discrete-ordinate-method radiative transfer in multiple scattering and emitting layered media. Applied Optics 27, 2502–2509.

Stofan, E. R., Elachi, C., Lunine, J. I., Lorenz, R. D., Stiles, B., Mitchell, K. L., Ostro, S., Soderblom, L., Wood, C., Zebker, H., Wall, S., Janssen, M., Kirk, R., Lopes, R., Paganelli, F., Radebaugh, J., Wye, L., Anderson, Y., Allison, M., Boehmer, R., Callahan, P., Encrenaz, P., Flamini, E., Francescetti, G., Gim, Y., Hamilton, G., Hensley, S., Johnson, W. T. K., Kelleher, K., Muhleman, D., Paillou, P., Picardi, G., Posa, F., Roth, L., Seu, R., Shaffer, S., Vetrella, S., West, R., Jan. 2007. The lakes of Titan. Nature 445, 61–64.

Thompson, W. R., Zollweg, J. A., Gabis, D. H., 1992. Vapor-liquid equilibrium thermodynamics of N_2 + CH_4: Model and Titan applications. Icarus 97, 187–199.

Tokano, T., Dec. 2009. Impact of seas/lakes on polar meteorology of Titan: Simulation by a coupled GCM-Sea model. Icarus 204, 619–636.

Tomasko, M. G., Archinal, B., Becker, T., Bézard, B., Bushroe, M., Combes, M., Cook, D., Coustenis, A., de Bergh, C., Dafoe, L. E., Doose, L., Douté, S., Eibl, A., Engel, S., Gliem, F., Grieger, B., Holso, K., Howington-Kraus, E., Karkoschka, E., Keller, H. U., Kirk, R., Kramm, R., Küppers, M., Lanagan, P., Lellouch, E., Lemmon, M., Lunine, J., McFarlane, E., Moores, J., Prout, G. M., Rizk, B., Rosiek, M., Rueffer, P., Schröder, S. E., Schmitt, B., See, C., Smith, P., Soderblom, L., Thomas, N., West, R., Dec. 2005. Rain, winds and haze during the Huygens probe's descent to Titan's surface. Nature 438, 765–778.

Turtle, E. P., Perry, J. E., Hayes, A. G., Lorenz, R. D., Barnes, J. W., McEwen, A. S., West, R. A., Del Genio, A. D., Barbara, J. M., Lunine, J. I., Schaller, E. L., Ray, T. L., Lopes, R. M. C., Stofan, E. R., Mar. 2011. Rapid and Extensive Surface Changes Near Titan's Equator: Evidence of April Showers. Science 331, 1414–.

Turtle, E. P., Perry, J. E., McEwen, A. S., Del Genio, A. D., Barbara, J., West, R. A., Dawson, D. D., Porco, C. C., Jan. 2009. Cassini imaging of Titan's high-latitude lakes, clouds, and south-polar surface changes. Geophys. Res. Lett. 36 (2), L02204.

Yung, Y. L., Allen, M., Pinto, J. P., Jul. 1984. Photochemistry of the atmosphere of Titan - Comparison between model and observations. Astrophys. J. Supp. Ser. 55, 465–506.

Appendix A. Spectral fitting methodology

Since z_s has discrete values for each layer in our radiative transfer model, we follow a brute force approach for optimization of this model parameter. For each particular observing geometry that corresponds to a pixel in the slit, we set z_s to each layer of the model and determine a goodness-of-fit parameter (e.g., as in Ádámkovics et al., 2010) that is the ratio of the mean absolute deviation of the residual in the spectrum for each channel, λ, relative to the observational uncertainty,

$$\widehat{\chi^2}(z_s) = \frac{1}{n}\sum_{i=1}^{n}\frac{|I_{\rm obs}(\lambda) - I_{\rm calc}(\lambda; z_s)|}{\sigma_{\rm obs}}. \tag{A.1}$$

A detailed analysis and determination of the observational uncertainty, $\sigma_{obs} = 0.002\, I/F$, is presented in Ádámkovics and Mitchell (2016). Values of $\widehat{\chi^2}(z_s)$ are calculated for z_s set to the altitude at the middle of each model layer from the surface up to 18 km. The discrete values of $\widehat{\chi^2}(z_s)$ are then fit with a second-order polynomial. The minimum in the polynomial is the optimized value for z_s for that pixel, and the 1σ uncertainty in the optimization is evaluated where the fit to $\widehat{\chi^2}(z_s) = 1$. The discrete values and fitting are illustrated for each spectrum in Figure A.1.

The optimization near the limb has a greater uncertainty than near the center of the disk. Near the limb, where the slant path through the atmosphere is largest and where spectral sensitivity to the surface is smallest, the optimization of z_s is asymmetric. In these regions the lower limit to the uncertainty in z_s is overestimated by the polynomial fit to the discrete values of $\widehat{\chi^2}(z_s)$. In these regions a total methane column that is in excess of saturation down to the surface could still be consistent with observations. This means that the spectra from near the limb could also be consistent with a warmer temperature profile than used in the model, or supersaturated conditions.

Appendix B. Test cases for retrievals

Here we explore how our retrieval results depend on our assumptions about haze variations near the surface and the atmospheric temperatures. We consider three scenarios for the meridional variation in haze below 10 km: (1) uniform haze, (2) haze opacity that increases linearly with latitude to the north, and (3) haze opacity that is arbitrarily variable to fit the observations.

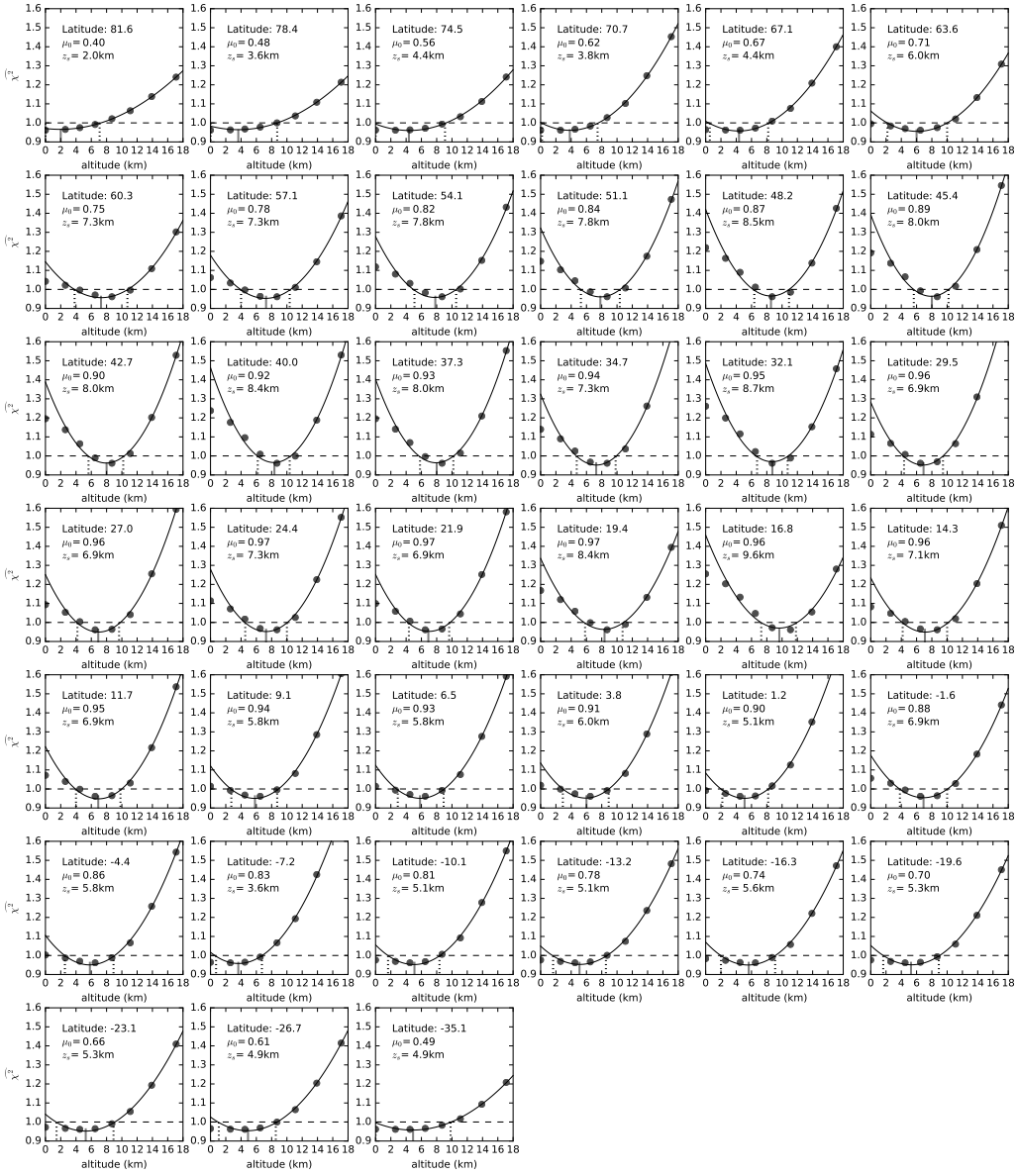

Figure A.1: The optimization for z_s presented in Figure 5, via the quality-of-fit parameter $\widehat{\chi^2}$, shown for each spectrum. The corresponding latitude, incidence angle $\mu_0 = \cos\theta_0$, and best fit z_s are given in each panel for each spectrum, where θ_0 is the angle between the incident ray path and the surface normal. The observations were performed on 17 July 2014 UT with a sub-observer longitude of 291°W, and a Sun-Titan-Observer phase angle of 5.4°, which is small enough that the emission angle μ_e differs from μ_0 by less than 0.01. $\widehat{\chi^2}$ is calculated for z_s in each layer of the model up to 18 km (data points), and a second-order polynomial is fit to the discrete values (solid curve) to determine the best fit value of z_s at the minimum of the fit (grey vertical line), with the 1σ uncertainties (dotted vertical lines) determined where $\widehat{\chi^2} = 1$ (horizontal dashed line) in the fit.

In the case of uniform haze, the aerosol optical depth is 0.22 below 10 km at 1.5 μm, whereas in the case of variable haze, the optical depth of aerosol increases linearly from 0.03 at 40°S to 0.10 at 80°N. The difference in optical depths is due to the different haze structure at higher altitudes in the two models (see Fig. 4 in Ádámkovics et al. (2016)). The total optical depth in both models is ∼0.5 at 40°S and increases monotonically to ∼0.9 at 70°N.

We consider an arbritary haze opacity in case (3) by starting with the nominal methane profile, fitting the spectra with a Levenberg-Marquardt optimization of the haze, and then determining the uncertainty in the methane saturation altitude as described in Appendix A. In practice, the Levenberg-Marquardt optimization fails for free parameters with discrete values, such as the saturation altitude z_s in the model, so the optimization cannot fit both parameters simultaneously. By starting with a nominal methane profile for the methane optimization, we are confining our analysis to a local minimum in the spectral fitting. We do not fully consider the global parameter space in this fitting, including, for example, whether supersaturated values of methane absorption can be balanced by significant enhancements in haze scattering. The goal of test case (3) is to evaluate our assumptions about either the uniform or linearly variable haze, and illustrate the saturation altitude sensitivity when we assume that the spectral variation is caused primarily by haze variation.

Retrievals of the saturation altitude, as well as the corresponding specific humidity and relative humidity at the surface, are presented for the various scenarios in Fig. B.2. The first and third rows are also shown in Fig. 6. In both of the cases where the haze is variable, the saturation altitudes and specific humidities do not show meridional variation, as is expected from the degeneracy in opacities. The retrieved saturation altitudes and humidities for both of these cases (bottom rows of Fig. B.2) are very similar to each other, and in both cases the retrievals are still marginally consistent with saturation to the surface at very high northern latitudes.

We also test for sensitivity to temperature by using the vertical temperature profile retrieved via radio occultation at 80°N during T57 by Schinder et al. (2012) for the four latitudes sampled north of 70°N. With cooler temperatures, the atmosphere holds less methane, so for a given increase in opacity (and associated methane column) methane must be saturated to lower altitudes. As illustrated in the top row of Fig. B.2 (and in Fig. 6), the saturation altitude decreases when retrieved assuming a polar temperature profile and constant haze opacity, and the trend from ∼45°N to the pole is

smooth. On the other hand, with constant temperatures, the retrievals yield a sudden increase in saturation altitudes at the four northernmost latitudes (second row of Fig. B.2), which we consider unphysical. In the case of variable haze (either arbitrarily or linearly-varying), haze opacity is independent of temperature and the choice of polar temperature profiles does not impact the retrievals.

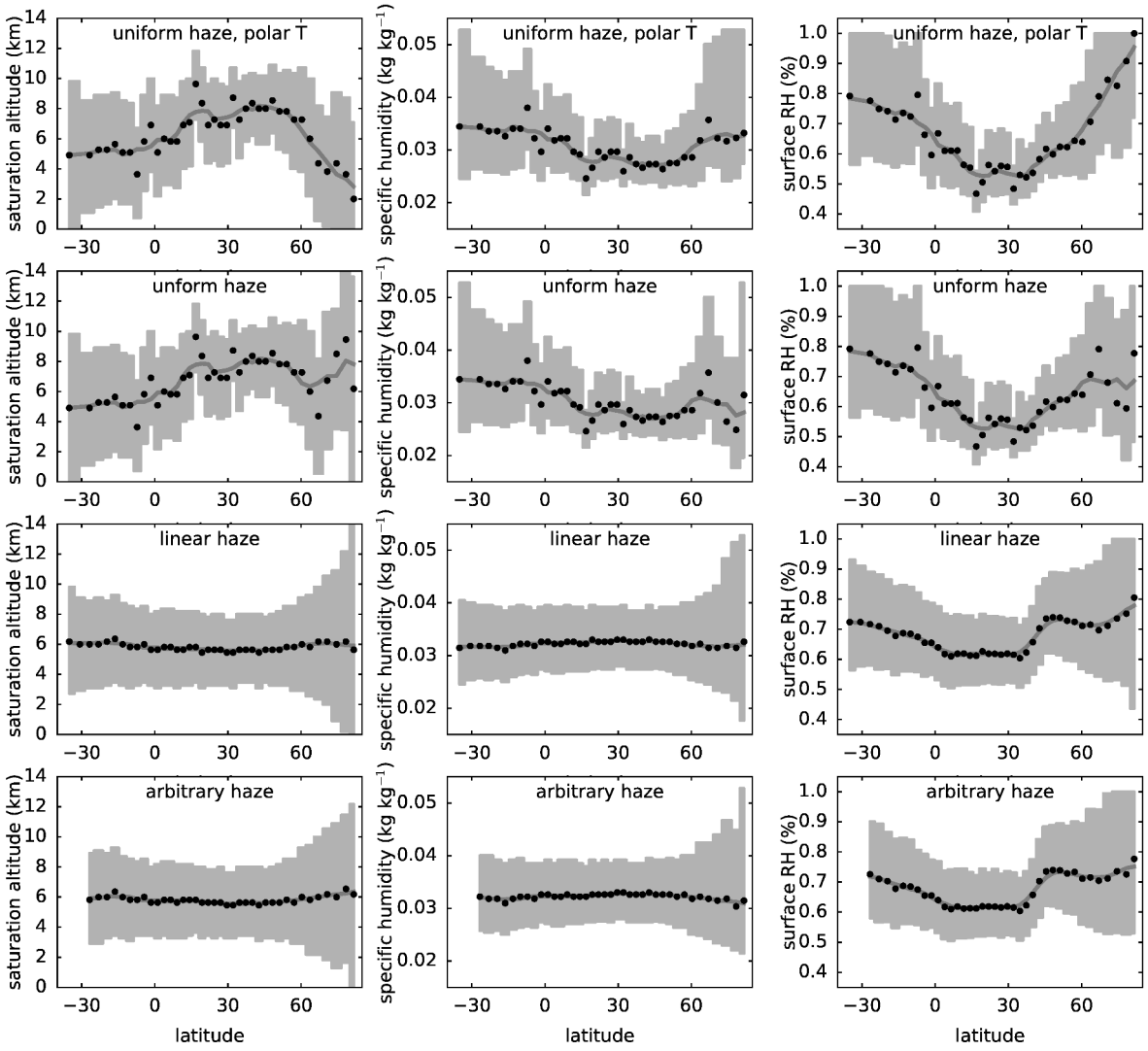

Figure B.2: The meridional variation of minimum saturation altitudes (left column), corresponding specific humidities (middle column), and associated surface-level relative humidities (right column) retrieved from the observations. Retrievals assuming a uniform haze and a polar temperature profile (see text) are in the top row. All other retrievals are shown assuming the temperature profile measured by the *Huygens* probe at all latitudes. Retrievals assuming a uniform haze are shown in the second row, retrievals assuming a linear haze variation are shown in the third row, and models assuming arbitrary haze opacities are shown in the bottom row.